

Cite this: *Nanoscale Adv.*, 2020, 2, 5883

Interfacial engineering with carbon–graphite– $\text{Cu}_\delta\text{Ni}_{1-\delta}\text{O}$ for ambient-air stable composite-based hole-conductor-free perovskite solar cells†

Yousheng Wang,¹ Yuzhao Yang,¹ Shaohang Wu, Cuiling Zhang, Zhen Wang, Jinlong Hu, Chong Liu,¹ Fei Guo¹ and Yaohua Mai^{1*}

Ambient air atmosphere is inimical to organic–inorganic halide perovskites and organic hole transport materials, and is, thus, necessarily avoided during device fabrication. To solve this issue, it is highly desirable to design stable perovskite-based composites and device configurations. Here, fully ambient-air and antisolvent-free-processed, stable and all-inorganic metal-oxide selective contact hole-conductor-free perovskite solar cells (HCF-PSCs) based on perovskite-based composites with an interfacial engineering strategy are reported. The formation of perovskite-based composites by interfacial engineering with carbon–graphite– $\text{Cu}_\delta\text{Ni}_{1-\delta}\text{O}$ not only improved interfacial contacts, charge extraction and transport but also passivated trap states of perovskite thin films and charge recombination at the interfaces. Thus, such perovskite composites with interfacial engineering-based HCF-PSCs without encapsulation showed excellent stability by sustaining 94% of initial PCE over 300 days under ambient conditions.

Received 13th October 2020
Accepted 1st November 2020

DOI: 10.1039/d0na00852d

rsc.li/nanoscale-advances

Introduction

Organic–inorganic halide perovskite (OIHP)-based solar cells have recently achieved an astonishing record-high power conversion efficiency (PCE) up to 25.5% just in a decade, which has endowed them with superb potential for next-generation low-cost, easy-to-fabricate, flexible, wearable and semi-transparent photovoltaics (PVs) in the near future.^{1–4} However, the poor stability of OIHPs and organic hole transport materials (OHTMs) owing to long time exposure to harsh environmental conditions (*i.e.*, moisture, air, light and heat stress) has threatened to hinder their widespread applications in optoelectronics and energy harvesting. To get closer to commercialization, the long-term operational stability and ambient-air scalable fabrication of perovskite solar cells (PSCs) are of utmost importance.^{5–8} Thus, more stable, printable and highly recyclable carbon-based mesoscopic hole-conductor-free PSCs (HCF-PSCs) may become one of the most promising perovskite-based PVs towards rapid commercialization. However, the efficiency of HCF-PSCs still largely lags behind as compared to that of small-molecule OHTM-based PSCs. The unsatisfactory

efficiency of HCF-PSCs is mainly ascribed to low hole transport efficiency, high charge recombination, undesired energy band diagram match and imperfect contacts at the interface of the perovskite/carbon electrode as well as poor carbon adhesion and insufficient incident light by carbon electrodes.^{9,10} In order to further improve the efficiency of HCF-PSCs, many efforts have been made for developing advanced and stable perovskite composites with organic or inorganic materials^{11–21} and designing novel device configurations with the interfacial engineering strategy.^{10,22–26}

The perovskite-based composition engineering with a mixed-cation/halide have significantly enhanced optical and electronic properties, electron–hole extraction and transport as well as intrinsic hybrid-perovskite structure stability.^{12–15,27–29} Han *et al.* pioneered HCF-PSCs based on mixed-cation or mixed-halide perovskites ((5-AVA)_xMA_{1-x}PbI_{3-y}(BF₄)_y, 5-AVA: 5-aminovaleric acid) by controlling the ratio of two cations or halides, thus endowing the corresponding cells with an improved PCE over 12% and operational stability.^{12,13} Interestingly, Grancini *et al.* showed that ultra-stable 2-dimensional/3-dimensional (2D/3D) perovskite-based composites (*i.e.*, (HOOC(CH₂)₄NH₃)₂PbI₄/MAPbI₃) could be formed *via* 5-AVAI composition engineering. The 2D/3D perovskite composite-based HCF-PSCs and modules have shown excellent stability over one year.¹⁵ For the development of perovskite composites with organic or inorganic materials, Wang *et al.*¹⁶ reported efficient and stable HCF-PSC-based perovskite-composites with a configuration of FTO/c-TiO₂/mp-TiO₂/MAPbI₃-NiO composite/Au. The MAPbI₃-NiO composites can effectively facilitate charge carrier generation by

Institute of New Energy Technology, College of Information Science and Technology, Jinan University, Guangzhou 510632, China. E-mail: wangys0120@jnu.edu.cn; yaohuamai@jnu.edu.cn

† Electronic supplementary information (ESI) available: FESEM images of Al₂O₃ and Cu_δNi_{1-δ}O NPs, device performance parameters in tables, *J*-*V* plots, EIS spectra, *J*-*V* plots of stability test and UV-vis absorption. See DOI: 10.1039/d0na00852d



improving photo-absorption and faster extraction of holes from perovskite to the Au electrode by NiO NPs. Hou *et al.*¹⁸ fabricated perovskite composite-based (*i.e.*, MAPbI₃-GuCl and guanidinium chloride) HCF-PSC with a higher open-circuit voltage (V_{oc}) of 1.02 V when compared to pristine MAPbI₃-based devices with only 0.88 V. By combining experimental and theoretical studies, the perovskite composites with organic or inorganic materials can significantly enhance the intrinsic stability of perovskite materials *via* strong chemical interactions and bonding or cross-linking as well as using the protective effect of perovskite grains by additive molecules. More importantly, the perovskite composites prepared with cost-effective and environmentally stable inorganic semiconductors, such as NiO nanostructures^{16,30–34} and carbon-based nanomaterials,^{35–39} have the potential for future commercialization.

The interfacial contacts and properties at the interfaces of the perovskite/electron-transport-layer (perovskite/ETL) and perovskite/electrode are critical for the photovoltaic performance and stability in HCF-PSCs. In particular, except for the degradation of OIHPs themselves, poor stability of the state-of-the-art PSCs can be attributed to interfacial collapse induced by the TiO₂ photocatalysis effect and charge accumulation at the TiO₂/perovskite interface,^{40,41} light-induced ion migration and segregation behavior,^{42–44} and formation of AuI₂⁻ or AgI₂⁻ because of the diffusion of Au or Ag into the perovskite.^{45,46} For improving the interface contact between the perovskite layer and top electrode, interfacial engineering has been proposed.^{22–26,47–49} Overall, the development of stable perovskite-based composites combined with proper materials and designing novel configuration with interfacial engineering are efficient strategies to achieve highly efficient and stable HCF-PSCs under ambient conditions.

In this study, we report fully-ambient-air and antisolvent-free-processed, highly efficient and stable HCF-PSCs with interfacial engineering-based perovskite composites. The perovskite composites (*i.e.*, Cu_δNi_{1-δ}O-MAPbI_{3-x}Cl_x, carbon-graphite (C-G)-Cu_δNi_{1-δ}O-MAPbI_{3-x}Cl_x and Al₂O₃-MAPbI_{3-x}Cl_x) were self-formed *via* a one-step deposition of the as-prepared MAPbI_{3-x}Cl_x-Cu_δNi_{1-δ}O mixed-solution on the stacked configuration of FTO/SnO₂/Al₂O₃/Cu_δNi_{1-δ}O/C-G-Cu_δNi_{1-δ}O, where SnO₂ is the ETL and Al₂O₃/Cu_δNi_{1-δ}O/C-G-Cu_δNi_{1-δ}O is used for interfacial engineering between ETL and the active layer (AL). It was found that Cu_δNi_{1-δ}O and C-G in the perovskite composites effectively facilitated charge extraction and transport as well as passivated the trap states of perovskite thin films, recombination and ion migration at the interfaces. Furthermore, the multi-stacked SnO₂/Al₂O₃-MAPbI_{3-x}Cl_x/Cu_δNi_{1-δ}O-MAPbI_{3-x}Cl_x/C-G-Cu_δNi_{1-δ}O-MAPbI_{3-x}Cl_x composite layer effectively reduced the photocurrent density loss and improved interfacial contacts. Finally, the HCF-PSCs based on perovskite composites with interfacial engineering yielded the best PCE of 14.78% with a V_{oc} of 0.95 V, J_{sc} of 23.85 mA cm⁻² and an FF of 65.23%. More importantly, such perovskite composites with interfacial engineering-based devices showed excellent air, photo- and thermal stability, which are attributed to moisture- and ion migration-sequestration by C-G and

strong chemical interactions between Cu_δNi_{1-δ}O and perovskite molecules.

Results and discussion

The surface morphologies of mesoporous Cu-doped NiO (Cu_δNi_{1-δ}O) and Al₂O₃, and the cross-sectional structure of FTO/SnO₂/Al₂O₃/Cu_δNi_{1-δ}O were examined *via* field emission scanning electron microscopy (FESEM), clearly showing uniform and mesoporous structures (Fig. S1†). Such thin-film morphologies of metal oxide nanoparticles (MONs) effectively facilitate the perovskite MAPbI_{3-x}Cl_x solution infiltration and increase the contact areas between perovskite molecules and mesoporous MONs (*i.e.*, Cu_δNi_{1-δ}O and Al₂O₃), leading to the formation of perovskite-MONs composites (*i.e.*, Cu_δNi_{1-δ}O-MAPbI_{3-x}Cl_x and Al₂O₃-MAPbI_{3-x}Cl_x). Besides, the surface morphologies of the as-formed C-G-Cu_δNi_{1-δ}O-MAPbI_{3-x}Cl_x composite film are also clearly observed in the FESEM image, as shown in Fig. 1a. Fig. 1d further verifies that the perovskite (MAPbI_{3-x}Cl_x) solution readily infiltrated into all the mesoporous layers of C-G-Cu_δNi_{1-δ}O, Cu_δNi_{1-δ}O, and Al₂O₃. It can be seen that all the layers are well-defined with good adhesion to one another, exhibiting the top electrode of Au, the AL of C-G-Cu_δNi_{1-δ}O-MAPbI_{3-x}Cl_x, the interfacial layer of Al₂O₃/Cu_δNi_{1-δ}O/C-G-Cu_δNi_{1-δ}O infiltrated with perovskite molecules and the ETL layer of SnO₂. Fig. 1b shows the device configuration of FTO/SnO₂/Al₂O₃-MAPbI_{3-x}Cl_x/Cu_δNi_{1-δ}O-MAPbI_{3-x}Cl_x/C-G-Cu_δNi_{1-δ}O-MAPbI_{3-x}Cl_x/Au, where the SnO₂ is the ETL and Al₂O₃/Cu_δNi_{1-δ}O/C-G-Cu_δNi_{1-δ}O is for interfacial engineering between ETL and AL. Such multi-layers of mesoporous configuration remarkably enhance the visible light-harvesting as well as improve J_{sc} (see Table 1 and Fig. 3a). Fig. 1c shows the energy band diagram and blocking properties in HCF-PSCs: (1) Cu_δNi_{1-δ}O and C-G in the AL have a suitable band energy alignment of the valence band (VB) (-5.3 eV) and (-5.0 eV),

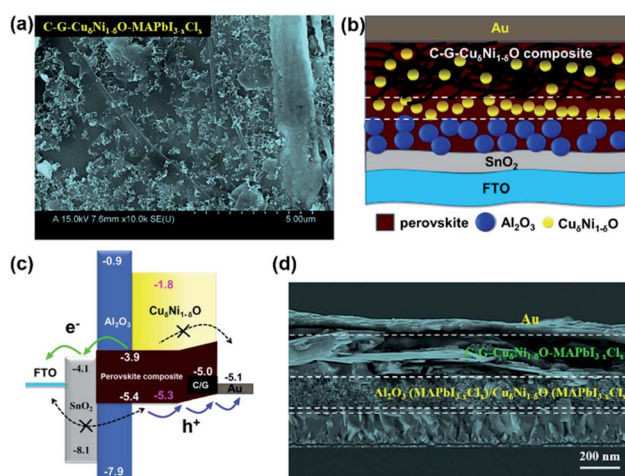


Fig. 1 (a) The surface morphology of the C-G-Cu_δNi_{1-δ}O-MAPbI_{3-x}Cl_x composite film, (b) device configuration, (c) schematic of the energy band diagram and blocking properties and (d) a cross-sectional SEM image for HCF-PSCs of FTO/SnO₂/Al₂O₃/Cu_δNi_{1-δ}O/C-G-Cu_δNi_{1-δ}O-MAPbI_{3-x}Cl_x/Au.



Table 1 Photovoltaic parameters of three types of HCF-PSCs: FTO/c-TiO₂/mp-TiO₂/Al₂O₃/Cu_δNi_{1-δ}O/C-G-MAPbI_{3-x}Cl_x/Au, FTO/SnO₂/Al₂O₃/Cu_δNi_{1-δ}O/C-G-MAPbI_{3-x}Cl_x/Au and FTO/SnO₂/Al₂O₃/Cu_δNi_{1-δ}O/C-G-Cu_δNi_{1-δ}O-MAPbI_{3-x}Cl_x/Au. *R_s*, *R₁* and *R₂* were measured at 250 mV-applied bias under one sunlight intensity in the range from 1 Hz to 300 kHz by electronic impedance spectroscopy (EIS) measurement

Device configuration	<i>V_{oc}</i> (V)	<i>J_{sc}</i> (mA cm ⁻²)	FF (%)	PCE (%)	<i>R_s</i> (Ω)	<i>R₁</i> (Ω)	<i>R₂</i> (Ω)
FTO/c-TiO ₂ /mp-TiO ₂ /Al ₂ O ₃ /Cu _δ Ni _{1-δ} O/C-G-MAPbI _{3-x} Cl _x /Au	0.88	20.97	55.30	10.21	14.5	346	748
FTO/SnO ₂ /Al ₂ O ₃ /Cu _δ Ni _{1-δ} O/C-G-MAPbI _{3-x} Cl _x /Au	0.90	23.01	57.12	11.83	12.2	338	956
FTO/SnO ₂ /Al ₂ O ₃ /Cu _δ Ni _{1-δ} O/C-G-Cu _δ Ni _{1-δ} O-MAPbI _{3-x} Cl _x /Au	0.95	23.85	65.23	14.78	10.8	245	1078

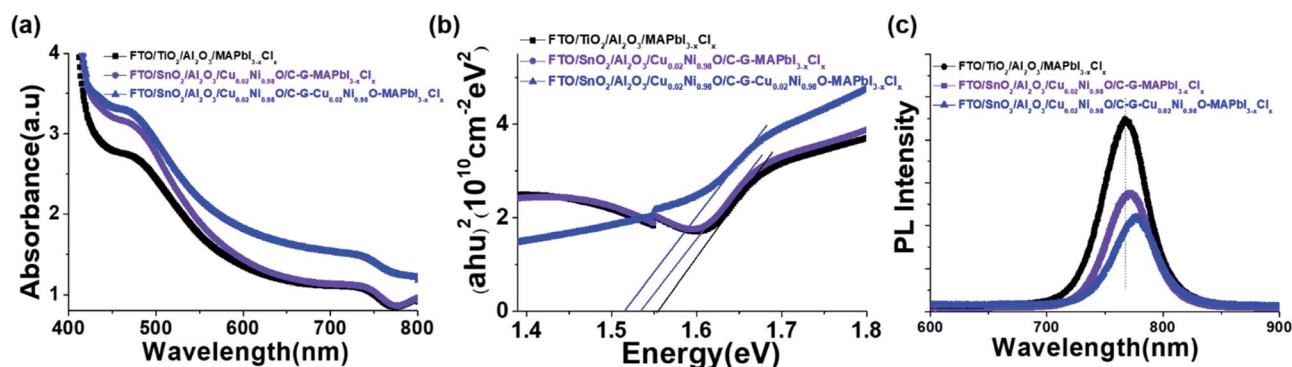


Fig. 2 (a) UV-vis spectra, (b) corresponding Tauc plots and (c) PL spectra for three films: FTO/TiO₂/Al₂O₃/MAPbI_{3-x}Cl_x (dark), FTO/SnO₂/Al₂O₃/Cu_δNi_{1-δ}O/C-G-MAPbI_{3-x}Cl_x (purple) and FTO/SnO₂/Al₂O₃/Cu_δNi_{1-δ}O/C-G-Cu_δNi_{1-δ}O-MAPbI_{3-x}Cl_x (blue).

which is quite close to that of perovskite MAPbI_{3-x}Cl_x (-5.4 eV), leading to fast hole transport; (2) the formation of the C-G-Cu_δNi_{1-δ}O-MAPbI_{3-x}Cl_x-graded heterojunction also enhances hole transport but efficiently blocks the electron going to the Au electrode due to electron blocking property of Cu_δNi_{1-δ}O with a high conduction band (CB) (-1.8 eV); (3) the wide-bandgap Al₂O₃ (~7 eV) plays an important role in hole-electron extraction and recombination suppression by avoiding direct contact between n-type SnO₂ and p-type Cu_δNi_{1-δ}O; (4) highly conductive C-G effectively improves the conductivity and work function of C-G-Cu_δNi_{1-δ}O composites; (5) defect density of perovskite films are suppressed by the C-G-Cu_δNi_{1-δ}O interface modification and strong chemical interactions or crosslinking between Cu_δNi_{1-δ}O and perovskite molecules.^{16,30-33,50,51} Upon illumination, the HCF device configuration probably four conduction paths are available for holes: direct transport to the Au electrode, transport to Cu_δNi_{1-δ}O to the Au electrode, transport to C-G to the Au electrode and transport to Cu_δNi_{1-δ}O to C-G and finally to the Au electrode. It is believed that SnO₂, Al₂O₃, Cu_δNi_{1-δ}O, and C-G can play individual roles in the effective electron and hole transport. Therefore, such a device configuration with perovskite composites and multi-layer interface engineering not only eliminates undesired interface energy disorder but also results in efficient charge separation and conduction in the AL and at the interfaces, leading to a remarkable improvement of device performance and stability.

To compare the optical and electronic properties of C-G-Cu_δNi_{1-δ}O-MAPbI_{3-x}Cl_x composites, C-G-MAPbI_{3-x}Cl_x composites and pristine perovskite MAPbI_{3-x}Cl_x films, we recorded ultraviolet-visible (UV-vis) spectra and photoluminescence (PL) spectra, as shown in Fig. 2. All films exhibit

remarkable light-harvesting absorption from 400 to 800 nm (Fig. 2a). Compared to the absorption of pristine perovskite MAPbI_{3-x}Cl_x and C-G-MAPbI_{3-x}Cl_x films, the C-G-Cu_δNi_{1-δ}O-MAPbI_{3-x}Cl_x composite film shows enhanced light absorption over the entire visible spectrum, resulting in the highest light-harvesting ability. More importantly, such a composite-based film shows an efficient PL quenching and red-shift toward longer wavelengths (Fig. 2c), which is attributed to a reduced band gap from 1.561 to 1.533 eV (Fig. 2b). The fast PL quenching, red-shift and reduced band gap indicate efficient carrier extraction and transport, and suppression of interfacial recombination and trap density, which can remarkably improve solar cell PV parameters (see Table 1 and Fig. 3a).

To evaluate the device performance of C-G-based HCF-PSCs based on perovskite composites with interfacial engineering, we fabricated three C-G-based devices: FTO/c-TiO₂/mp-TiO₂/Al₂O₃/Cu_δNi_{1-δ}O/C-G-MAPbI_{3-x}Cl_x/Au (device A, Fig. S2†), FTO/SnO₂/Al₂O₃/Cu_δNi_{1-δ}O/C-G-MAPbI_{3-x}Cl_x/Au (device B, Fig. S3†), and FTO/SnO₂/Al₂O₃/Cu_δNi_{1-δ}O/C-G-Cu_δNi_{1-δ}O-MAPbI_{3-x}Cl_x/Au (device C, Fig. 1d). Devices B and C incorporated SnO₂ to replace TiO₂ ETL and device C used the C-G-Cu_δNi_{1-δ}O-MAPbI_{3-x}Cl_x composite in AL. It was confirmed that the Cu_δNi_{1-δ}O optoelectronic properties greatly depend on Cu doping concentrations.¹⁷ Herein, we scrutinized the PV performance of the device A for different concentrations of Cu doping and obtained the best PCE with an optimal content of δ = 0.02 (Fig. S2c and Table S1†). Besides, the thickness of SnO₂ and the concentration of C-G-Cu_δNi_{1-δ}O composites in HCF-PSCs were also optimized, as shown in Fig. S3c and Table S3†. In conclusion, the incorporation of the C-G-Cu_δNi_{1-δ}O-MAPbI_{3-x}Cl_x composite in AL together with SnO₂, ETL and Al₂O₃/Cu_δNi_{1-δ}O/C-G-Cu_δNi_{1-δ}O



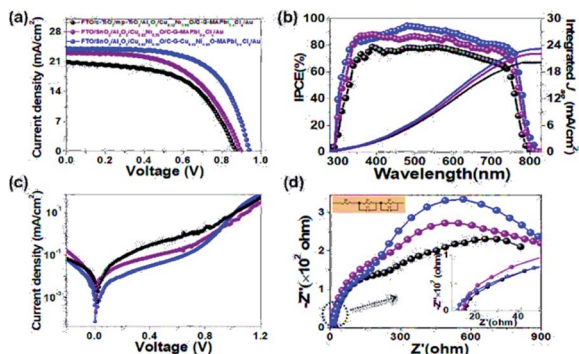


Fig. 3 (a) J - V curves, (b) IPCE spectra with integrated J_{sc} , (c) dark current, (d) EIS spectra (inset is the enlarged area for dash curve) for HCF-PSCs: FTO/c-TiO₂/mp-TiO₂/Al₂O₃/Cu_δNi_{1-δ}O/C-G-MAPbI_{3-x}Cl_x/Au (black), FTO/SnO₂/Al₂O₃/Cu_δNi_{1-δ}O/C-G-MAPbI_{3-x}Cl_x/Au (purple) and FTO/SnO₂/Al₂O₃/Cu_δNi_{1-δ}O/C-G-Cu_δNi_{1-δ}O-MAPbI_{3-x}Cl_x/Au (blue).

interfacial engineering layers showed the overall best performance for the HCF devices (*i.e.*, a PCE of 14.78% with a V_{oc} of 0.95 V, J_{sc} of 23.85 mA cm⁻², and FF of 65%, Table 1). Such enhancement of V_{oc} and J_{sc} is ascribed to the reduced defect-related losses and trap density in materials, desirable energy-level alignment with almost no electron-transport-barrier SnO₂ as ETL, efficient blocking properties of Al₂O₃ and Cu_δNi_{1-δ}O, and formation of a graded heterojunction by perovskite composites. It can be noted that the incident-photon-to-current-efficiency (IPCE) spectrum of the HCF-champion cell (device C) shows the strongest light absorption over a broad wavelength from 350 to 780 nm than that of device A and device B (Fig. 3b). Moreover, the integrated J_{sc} of the HCF-champion cell calculated from the IPCE spectrum was 23.21 mA cm⁻², which is in good agreement with the measured J - V curve (23.85 mA cm⁻²). Fig. 3c clearly shows that the dark current density of the C-G-Cu_δNi_{1-δ}O-MAPbI_{3-x}Cl_x composite-based device is almost one order of magnitude lower than that of the pristine MAPbI_{3-x}Cl_x perovskite-based device. Note that device C shows the lowest series-resistant R_s and charge transfer resistance R_1 of 10.8 and 245 Ω, and highest recombination resistance R_2 of 1078 Ω, which were obtained *via* electronic impedance spectroscopy (EIS) measurements (Fig. 3d and Table 1). Such results indicate that the C-G-Cu_δNi_{1-δ}O-MAPbI_{3-x}Cl_x composite films can not only improve interfacial contacts, charge extraction and transport but also lower the current leakage and charge recombination as well as increase the shunt resistance and longer carrier lifetime.

It was found that compared to TiO₂ ETL devices (device A, black curve), the SnO₂ ETL devices (devices B (red) and C (blue) in Fig. 3a) showed the remarkable enhancement of PCE and photo-stability (Fig. S3d and S5†). Furthermore, we examined how light soaking time affects the PV performance of HCF devices and found that the TiO₂-based device A increased its PV parameters for 90 s and then were gradually decreasing (Fig. S2d and Table S2†). However, the SnO₂-based devices B and C resulted in the substantial improvement of photovoltaic parameters as a function of light soaking time and was

stabilized after 200 s (Fig. S3d, S4b, S5, Tables S4 and S6†). Thermal stability is another challenge towards the rapid commercialization of PSCs. Compared to the pristine MAPbI_{3-x}Cl_x with spiro-OMeTAD device (control device), C-G-Cu_δNi_{1-δ}O-MAPbI_{3-x}Cl_x with interfacial engineering-based HCF-PSCs shows excellent thermal-stability at 85 °C under ambient conditions (45–50% humidity) (Fig. S6†). In particular, all PV parameters of the pristine MAPbI_{3-x}Cl_x with HTM spiro-OMeTAD-based cell showed severely deteriorated thermal stability after 120 h, *i.e.*, original PCEs decreased from 18.02% to 7.71% (only retaining 42.8%, Table S7 and Fig. S7a†). However, C-G-Cu_δNi_{1-δ}O-MAPbI_{3-x}Cl_x based on interfacial engineering HCF-PSCs sustained its stability over 120 h by retaining ~97.8% of its original V_{oc} , ~92.6% of J_{sc} , ~99.1% of FF and ~89.8% of PCE at 85 °C in an ambient environment (45–50% humidity) (Fig. S7b and Table S8†). Furthermore, we examined UV-vis spectrum performance as a function of time for FTO/SnO₂/MAPbI_{3-x}Cl_x/spiro-OMeTAD and FTO/SnO₂/Al₂O₃/Cu_δNi_{1-δ}O/C-G-Cu_δNi_{1-δ}O-MAPbI_{3-x}Cl_x films at 85 °C heating in ambient air (humidity 45–50%). The UV-vis spectrum performance clearly shows that the pristine MAPbI_{3-x}Cl_x with the spiro-OMeTAD film totally changed to PbI₂ after 20 days. Adversely, the C-G-Cu_δNi_{1-δ}O-MAPbI_{3-x}Cl_x-based film had almost no change (Fig. S8†). To examine the long-term stability of the HCF devices based on C-G-Cu_δNi_{1-δ}O-MAPbI_{3-x}Cl_x with Al₂O₃/Cu_δNi_{1-δ}O/C-G-Cu_δNi_{1-δ}O interfacial engineering, the target device fabricated by the antisolvent-free strategy was stored under ambient conditions without any encapsulation. Fig. 4 shows the control (pristine MAPbI_{3-x}Cl_x with spiro-OMeTAD-based cell) and the target device (C-G-Cu_δNi_{1-δ}O-MAPbI_{3-x}Cl_x-based HCF-cell) of long-term stability as a function of storage days in terms of the normalized performance parameters, *i.e.* V_{oc} (a), J_{sc} (b), FF (c) and PCE (d). Compared to the control device, it can be clearly seen that the normalized performance parameters in the target device are almost not changed in 300 d. More importantly, the target device sustained its stability over 300 days by retaining ~94% of PCE in an

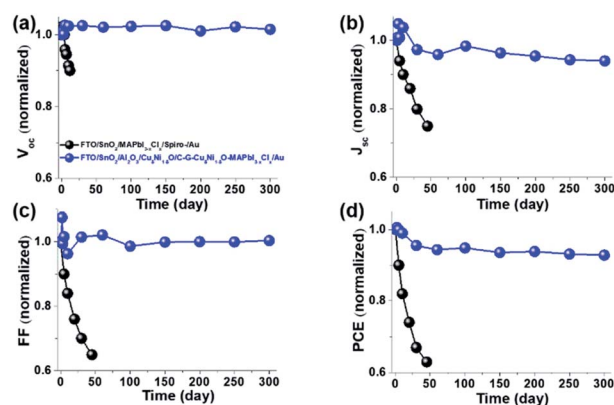


Fig. 4 Long-term stability of FTO/SnO₂/MAPbI_{3-x}Cl_x/spiro-OMeTAD/Au (black) and FTO/SnO₂/Al₂O₃/Cu_δNi_{1-δ}O/C-G-Cu_δNi_{1-δ}O-MAPbI_{3-x}Cl_x/Au under ambient conditions (45–50% humidity and 25–30 °C).



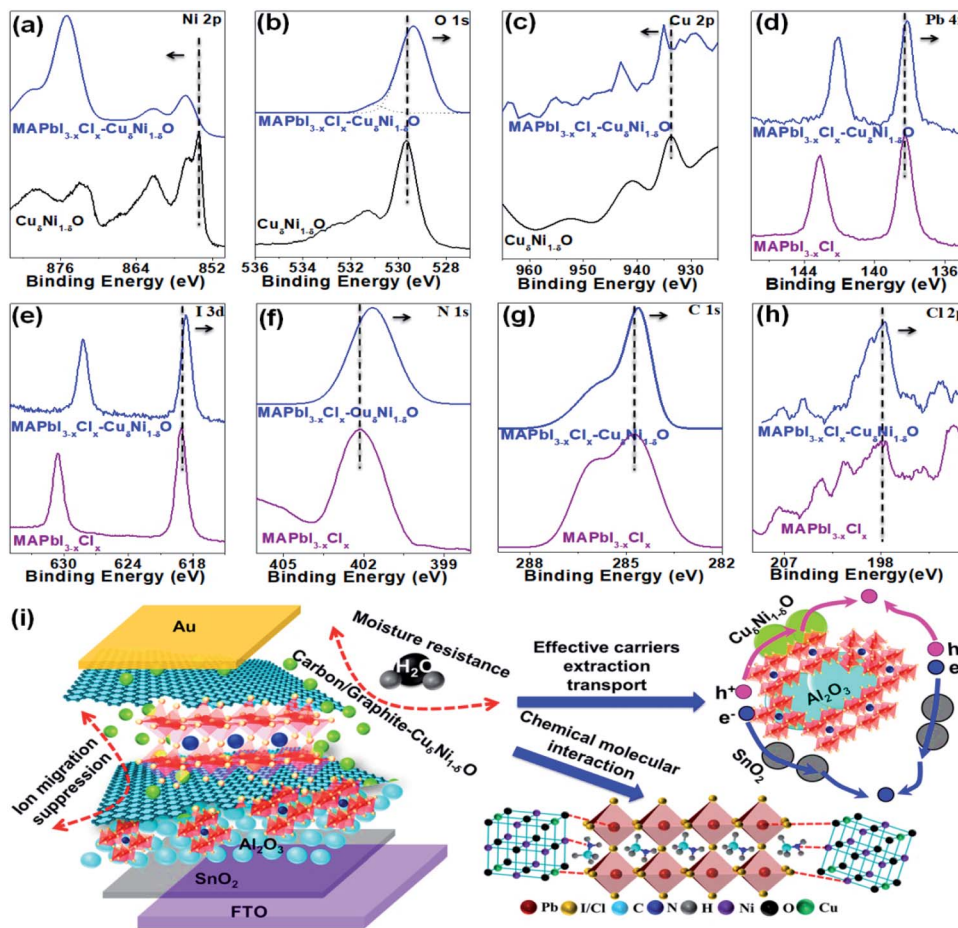


Fig. 5 X-ray photoelectron spectroscopy (XPS) spectra of $\text{MAPbI}_{3-x}\text{Cl}_x$ and $\text{MAPbI}_{3-x}\text{Cl}_x\text{-Cu}_\delta\text{Ni}_{1-\delta}\text{O}$ films: (a) Ni 2p, (b) O 1s, (c) Cu 2p, (d) Pb 4f, (e) I 3d, (f) N 1s, (g) C 1s and (h) Cl 2p. (i) Stability, carrier working mechanisms, and possibility of chemical bonding Ni–I, Ni–Pb, Pb–O–Pb and N–Ni between $\text{Cu}_\delta\text{Ni}_{1-\delta}\text{O}$ and perovskite material.

ambient environment (45–50% humidity) (Fig. S9 and Table S9†).

By examining XPS data (Fig. 5) on both pristine $\text{MAPbI}_{3-x}\text{Cl}_x$ and composite-based $\text{Cu}_\delta\text{Ni}_{1-\delta}\text{O-MAPbI}_{3-x}\text{Cl}_x$ films, the core levels of all components in the $\text{Cu}_\delta\text{Ni}_{1-\delta}\text{O-MAPbI}_{3-x}\text{Cl}_x$ film (*i.e.*, O 1s, Pb 4f, I 3d, N 1s, C 1s and Cl 2p) showed a substantial shift towards a lower binding energy compared to the pristine $\text{MAPbI}_{3-x}\text{Cl}_x$ film. Interestingly, the core level of Ni 2p and Cu 2p showed a slight shift towards a higher binding energy, where the nitrogen and iodide or chloride ligands from the MA cation might serve as a ligand bridge to form Ni/Cu–N and Ni/Cu–I or Ni/Cu–Cl bonds, respectively. From the XPS data, it can be concluded that there is a presence of strong chemical interaction and chemical bonding between $\text{Cu}_\delta\text{Ni}_{1-\delta}\text{O}$ and perovskite, as shown in Fig. 5. In conclusion, such improvement is mainly attributed to the effect of $\text{Cu}_\delta\text{Ni}_{1-\delta}\text{O}$ and C–G in the perovskite-based composites, which can effectively facilitate charge extraction and transport and interfacial contacts as well as passivation of trap states and recombination in perovskite thin films and at interfaces (also see Fig. 5). The strong chemical interactions and bonding between perovskite and $\text{Cu}_\delta\text{Ni}_{1-\delta}\text{O}$ elements as well as the presence of C–G in composites also

enhance the intrinsic stability of the perovskite materials and interfacial degradation.^{16,30–32,52} Moreover, the lattice constant of graphite ($\alpha = 2.46 \text{ \AA}$) is less than the ionic diameter of I/Cl ($d = 4.28 \text{ \AA}/3.62 \text{ \AA}$), which significantly suppresses the halide migration towards the top electrode. In addition, the multi-stacked configuration of $\text{SnO}_2/\text{Al}_2\text{O}_3/\text{Cu}_\delta\text{Ni}_{1-\delta}\text{O}/\text{C-G-Cu}_\delta\text{Ni}_{1-\delta}\text{O-MAPbI}_{3-x}\text{Cl}_x$ can effectively reduce the photocurrent density loss and improve interfacial contacts between perovskite and other layers. Such multi-layer configuration can also effectively improve device air-stability by protecting perovskite molecules from moisture resistance by C–G, and deprotonation and decomposition due to reduction with superoxide (O_2^-) (Fig. 5). In all, the combined perovskite-based composites and interfacial engineering can lead to substantial performance improvements and operational stability in HCF-PSCs.

Conclusions

In summary, we have achieved fully-ambient-air and antisolvent-free-processed stable hole-conductor-free perovskite solar cells (HCF-PSCs) based on perovskite composites with carbon-graphite (C–G)– $\text{Cu}_\delta\text{Ni}_{1-\delta}\text{O}$ interfacial engineering.



With the substantial improvement in the perovskite properties, energy-level alignment at the p-type interface between perovskite and C-G-Cu_δNi_{1-δ}O and their interfacial contacts, the perovskite composites with interfacial engineering-based HCF-PSCs yielded a PCE of 14.78% and excellent operational stability. We believe that metal oxides and carbon-based perovskite composites and interfacial engineering can pave the way for designing efficient, large-scale and stable PSCs.

Experimental section

Material preparation

The synthesis of CH₃NH₃I (methylammonium iodide, MAI) was described in our previous works.¹⁶ The preparation of the SnO₂ precursor, Al₂O₃ and Cu_δNi_{1-δ}O NP solutions can be found in our previous works.³⁰⁻³³ To prepare a solution of MAPbI_{3-x}Cl_x-Cu_δNi_{1-δ}O composite, 100 μL 1.5 wt% Cu_δNi_{1-δ}O (2 at% Cu doping) dispersion was added to the perovskite MAPbI_{3-x}Cl_x solution contained by mixing 475 mg MAI and 222 mg lead(II) chloride (PbCl₂, 99.999%, Sigma-Aldrich) and 76 mg lead(II) acetate trihydrate (Pb(CH₃CO₂)₂·3H₂O, 99.999%, Sigma-Aldrich) in 1 mL dimethylformamide, followed by ultrasonication for 30 min and continuously stirring for 24 h under ambient conditions (45–50% humidity and 25–30 °C).

Device fabrication

All the fabrication processes of PSCs were carried out *via* antisolvent-free and ambient-air processes (45–50% humidity and 25–30 °C). The SnO₂ precursor, Al₂O₃ and Cu_δNi_{1-δ}O NP solutions were spin-coated sequentially on a cleaned FTO substrate at 4000 rpm for 40 s; next, the C-G-Cu_δNi_{1-δ}O composite solution was drop-casted at 6000 rpm on FTO/SnO₂/Al₂O₃/Cu_δNi_{1-δ}O substrates; after that, each step was followed by annealing at 250 °C for 10 min. The pre-heated MAPbI_{3-x}Cl_x-Cu_δNi_{1-δ}O mixed solution at 130 °C was then spin-coated on the FTO/SnO₂/Al₂O₃/Cu_δNi_{1-δ}O/(C-G-Cu_δNi_{1-δ}O composite) at 1500 rpm for 30 s, followed by annealing at 130 °C for 1.5 h. Finally, Au electrodes were deposited through a shadow mask in a thermal evaporator (QHV-R53) under a high vacuum.

Characterization

The absorption properties and elemental compositions and chemical and electron states of perovskite composites were analyzed with ultraviolet-visible (UV-vis, DektakXT) spectroscopy and X-ray photoelectron spectroscopy (XPS). The perovskite device configuration was examined *via* field emission scanning electron microscopy (FE-SEM, FEI Apreo LoVac). Perovskite composite bonds were analyzed *via* Fourier transform infrared (IR) transmittance measurements. The performance parameters of PSCs were measured with a solar simulator with a source meter (Keithley series 2400) at 100 mW cm⁻² under AM 1.5 illumination, which was calibrated by a silicon reference cell. The dimension of the tested solar cells was 3 cm × 3 cm. The device performances were examined with a 0.16 cm² mask/aperture. To understand the electrical characteristics of the devices, electronic impedance spectroscopy

(EIS) was performed at 250 mV applied-bias under one sunlight intensity in the range from 1 Hz to 300 kHz.

Conflicts of interest

There are no conflicts to declare.

Acknowledgements

This work was supported by the Fundamental Research Funds for the Central Universities (No. 21620347) and startup fund for young talented person program (No. 88016105) from Jinan University.

References

- 1 NREL, <https://www.nrel.gov/pv/assets/pdfs/best-research-cell-efficiencies.20200925.pdf>, accessed on September 25, 2020.
- 2 B. Cai, Y. Xing, Z. Yang, W.-H. Zhang and J. Qiu, *Energy Environ. Sci.*, 2013, **6**, 1480–1485.
- 3 E. H. Jung, N. J. Jeon, E. Y. Park, C. S. Moon, T. J. Shin, T.-Y. Yang, J. H. Noh and J. Seo, *Nature*, 2019, **567**, 511–515.
- 4 X. Meng, Z. Cai, Y. Zhang, X. Hu, Z. Xing, Z. Huang, Z. Huang, Y. Cui, T. Hu, M. Su, X. Liao, L. Zhang, F. Wang, Y. Song and Y. Chen, *Nat. Commun.*, 2020, **11**, 3016.
- 5 S. S. Mai, H. Kim, S. E. Shim and C. K. Hong, *Nanoscale*, 2016, **8**, 19189–19194.
- 6 P. Wang, Y. Wu, B. Cai, Q. Ma, X. Zheng and W.-H. Zhang, *Adv. Funct. Mater.*, 2019, **29**, 1807661.
- 7 J. Hu, C. Wang, S. Qiu, Y. Zhao, E. Gu, L. Zeng, Y. Yang, C. Li, X. Liu, K. Forberich, C. J. Brabec, M. K. Nazeeruddin, Y. Mai and F. Guo, *Adv. Energy Mater.*, 2020, **10**, 2000173.
- 8 M. He, B. Li, X. Cui, B. Jiang, Y. He, Y. Chen, D. O'Neil, P. Szymanski, M. A. El-Sayed, J. Huang and Z. Lin, *Nat. Commun.*, 2017, **8**, 16045.
- 9 H. Chen and S. Yang, *Adv. Mater.*, 2017, **29**, 1603994.
- 10 K. Lee, J. Kim, H. Yu, J. W. Lee, C.-M. Yoon, S. K. Kim and J. Jang, *J. Mater. Chem. A*, 2018, **6**, 24560–24568.
- 11 S. He, L. Qiu, D.-Y. Son, Z. Liu, E. J. Juarez-Perez, L. K. Ono, C. Stecker and Y. Qi, *ACS Energy Lett.*, 2019, **4**, 2032–2039.
- 12 Y. Sheng, A. Mei, S. Liu, M. Duan, P. Jiang, C. Tian, Y. Xiong, Y. Rong, H. Han and Y. Hu, *J. Mater. Chem. A*, 2018, **6**, 2360–2364.
- 13 A. Mei, X. Li, L. Liu, Z. Ku, T. Liu, Y. Rong, M. Xu, M. Hu, J. Chen, Y. Yang, M. Grätzel and H. Han, *Science*, 2014, **345**, 295–298.
- 14 P. Liu, Y. Gong, Y. Xiao, M. Su, S. Kong, F. Qi, H. Zhang, S. Wang, X. Sun, C. Wang and X.-Z. Zhao, *Chem. Commun.*, 2019, **5**, 218–221.
- 15 G. Grancini, C. Roldán-Carmona, I. Zimmermann, E. Mosconi, X. Lee, D. Martineau, S. Narbey, F. Oswald, F. De Angelis, M. Grätzel and M. K. Nazeeruddin, *Nat. Commun.*, 2017, **8**, 15684.
- 16 Y. Wang, W.-Y. Rho, H.-Y. Yang, T. Mahmoudi, S. Seo, D.-H. Lee and Y.-B. Hahn, *Nano Energy*, 2016, **27**, 535–544.



- 17 Y. Sheng, Y. Hu, A. Mei, P. Jiang, X. Hou, M. Duan, L. Hong, Y. Guan, Y. Rong, Y. Xiong and H. Han, *J. Mater. Chem. A*, 2016, **4**, 16731–16736.
- 18 X. Hou, Y. Hu, H. Liu, A. Mei, X. Li, M. Duan, G. Zhang, Y. Rong and H. Han, *J. Mater. Chem. A*, 2017, **5**, 73–78.
- 19 I. Zimmermann, P. Gratia, D. Martineau, G. Grancini, J.-N. Audinot, T. Wirtz and M. K. Nazeeruddin, *J. Mater. Chem. A*, 2019, **7**, 8073–8077.
- 20 H. Zhang, H. Wang, S. T. Williams, D. Xiong, W. Zhang, C.-C. Chueh, W. Chen and A. K.-Y. Jen, *Adv. Mater.*, 2017, **29**, 1606608.
- 21 W.-Q. Wu, Q. Wang, Y. Fang, Y. Shao, S. Tang, Y. Deng, H. Lu, Y. Liu, T. Li, Z. Yang, A. Gruverman and J. Huang, *Nat. Commun.*, 2018, **9**, 1625.
- 22 Y. Xiong, X. Zhu, A. Mei, F. Qin, S. Liu, S. Zhang, Y. Jiang, Y. Zhou and H. Han, *Sol. RRL*, 2018, **2**, 1800002.
- 23 J. Liu, Q. Zhou, N. K. K. Thein, L. Tian, D. Jia, E. M. J. Johansson and X. Zhang, *J. Mater. Chem. A*, 2019, **7**, 13777–13786.
- 24 E. Avigad and L. Etgar, *ACS Energy Lett.*, 2018, **3**, 2240–2245.
- 25 B. Li, Y. Zhang, L. Zhang and L. Yin, *Adv. Mater.*, 2017, **29**, 1701221.
- 26 X. Zheng, H. Chen, Q. Li, Y. Yang, Z. Wei, Y. Bai, Y. Qiu, D. Zhou, K. S. Wong and S. Yang, *Nano Lett.*, 2017, **17**, 2496–2505.
- 27 M. Saliba, T. Matsui, K. Domanski, J.-Y. Seo, A. Ummadisingu, S. M. Zakeeruddin, J.-P. Correa-Baena, W. R. Tress, A. Abate, A. Hagfeldt and M. Grätzel, *Science*, 2016, **354**, 206–209.
- 28 Q. Tai, P. You, H. Sang, Z. Liu, C. Hu, H. L. W. Chan and F. Yan, *Nat. Commun.*, 2016, **7**, 11105.
- 29 A. D. Jodlowski, C. Roldan-Carmona, G. Grancini, M. Salado, M. Ralairisoa, S. Ahmad, N. Koch, L. Camacho, G. de Miguel and M. K. Nazeeruddin, *Nat. Energy*, 2017, **2**, 972–979.
- 30 Y. Wang, T. Mahmoudi, W.-Y. Rho, H.-Y. Yang, S. Seo, K. S. Bhat, R. Ahmad and Y.-B. Hahn, *Nano Energy*, 2017, **40**, 408–417.
- 31 Y. Wang, T. Mahmoudi, H.-Y. Yang, K. S. Bhat, J.-Y. Yoo and Y.-B. Hahn, *Nano Energy*, 2018, **49**, 59–66.
- 32 Y. Wang, T. Mahmoudi, W.-Y. Rho and Y.-B. Hahn, *Nano Energy*, 2019, **64**, 103964.
- 33 Y. Wang, T. Mahmoudi and Y.-B. Hahn, *Adv. Energy Mater.*, 2020, **10**, 2000967.
- 34 S. S. Mali, H. Kim, H. H. Kim, S. E. Shim and C. K. Hong, *Mater. Today*, 2018, **21**, 483–500.
- 35 H.-L. Hsu, H.-T. Hsiao, T.-Y. Juang, B.-H. Jiang, S.-C. Chen, R.-J. Jeng and C.-P. Chen, *Adv. Energy Mater.*, 2018, **8**, 1802323.
- 36 T. Mahmoudi, Y. Wang and Y.-B. Hahn, *ACS Energy Lett.*, 2019, **4**, 235–241.
- 37 T. Mahmoudi, Y. Wang and Y.-B. Hahn, *Nano Energy*, 2018, **47**, 51–65.
- 38 T. Mahmoudi, S. Seo, H.-Y. Yang, W.-Y. Rho, Y. Wang and Y.-B. Hahn, *Nano Energy*, 2016, **28**, 179–187.
- 39 Y. Liang, Y. Wang, C. Mu, S. Wang, X. Wang, D. Xu and L. Sun, *Adv. Energy Mater.*, 2018, **8**, 1701159.
- 40 W. Li, W. Zhang, S. V. Reenen, R. J. Sutton, J. Fan, A. A. Haghighirad, M. B. Johnston, L. Wang and H. J. Snaith, *Energy Environ. Sci.*, 2016, **9**, 490–498.
- 41 T. Leijtens, G. E. Eperon, S. Pathak, A. Abate, M. M. Lee and H. J. Snaith, *Nat. Commun.*, 2013, **4**, 2885.
- 42 P. Calado, A. M. Telford, D. Bryant, X. Li, J. Nelson, B. C. O'Regan and P. R. F. Barnes, *Nat. Commun.*, 2016, **7**, 13831.
- 43 Z. Li, C. Xiao, Y. Yang, S. P. Harvey, D. H. Kim, J. A. Christians, M. Yang, P. Schulz, S. U. Nanayakkara, C.-S. Jiang, J. M. Luther, J. J. Berry, M. C. Beard, M. M. Al-Jassim and K. Zhu, *Energy Environ. Sci.*, 2017, **10**, 1234–1242.
- 44 S. G. Motti, D. Meggiolaro, A. J. Barker, E. Mosconi, C. A. R. Perini, J. M. Ball, M. Gandini, M. Kim, F. D. Angelis and A. Petrozza, *Nat. Photonics*, 2019, **13**, 532–539.
- 45 L. Liang, Y. Cai, X. Li, M. K. Nazeeruddin and P. Gao, *Nano Energy*, 2018, **52**, 211–238.
- 46 H. Back, G. Kim, J. Kim, J. Kong, T. K. Kim, H. Kang, H. Kim, J. Lee, S. Lee and K. Lee, *Energy Environ. Sci.*, 2016, **9**, 1258–1263.
- 47 M. Duan, C. Tian, Y. Hu, A. Mei, Y. Rong, Y. Xiong, M. Xu, Y. Sheng, P. Jiang, X. Hou, X. Zhu, F. Qin and H. Han, *ACS Appl. Mater. Interfaces*, 2017, **9**, 31721–31727.
- 48 Z. Wu, Z. Liu, Z. Hu, Z. Hawash, L. Qiu, Y. Jiang, L. K. Ono and Y. Qi, *Adv. Mater.*, 2019, **31**, 1804284.
- 49 Q.-Q. Chu, Z. Sun, B. Ding, K.-S. Moon, G.-J. Yang and C.-P. Wong, *Nano Energy*, 2020, **77**, 105110.
- 50 G. D. Tainter, T. Horantner, L. M. Pazos-Outon, R. D. Lamboll, H. Abolins, T. Leijtens, S. Mahesh, R. H. Friend, H. J. Snaith, H. J. Joyce and F. Deschler, *Joule*, 2019, **3**, 1301–1313.
- 51 P. Jiang, Y. Xiong, M. Xu, A. Mei, Y. Sheng, L. Hong, T. W. Jones, G. J. Wilson, S. Xiong, D. Li, Y. Hu, Y. Rong and H. Han, *J. Phys. Chem. C*, 2018, **122**, 16481–16487.
- 52 T. Mahmoudi, Y. Wang and Y.-B. Hahn, *Adv. Energy Mater.*, 2020, **10**, 1903369.

